

Feedback control of slowly-varying transient growth by an array of plasma actuators

Ronald E. Hanson,¹ Kyle M. Bade,² Brandt A. Belson,³
Philippe Lavoie,^{1,a)} Ahmed M. Naguib,² and Clarence W. Rowley³

¹*Institute for Aerospace Studies, University of Toronto, Toronto, Ontario M3H 5T6, Canada*

²*Department of Mechanical Engineering, Michigan State University, East Lansing, Michigan 48824-1226, USA*

³*Department of Mechanical and Aerospace Engineering, Princeton University, Princeton, New Jersey 08544-5263, USA*

(Received 23 July 2013; accepted 13 January 2014; published online 5 February 2014)

Closed-loop feedback control of boundary layer streaks embedded in a laminar boundary layer and experiencing transient growth, which is inherent to bypass boundary layer transition, is experimentally investigated. Streaky disturbances are introduced by a spanwise array of cylindrical roughness elements, and a counter disturbance is provided by a spanwise array of plasma actuators, which are capable of generating spanwise-periodic counter rotating vortices in the boundary layer. Feedback is provided by a spanwise array of shear stress sensors. An input/output model of the system is obtained from measurements of the boundary layer response to steady forcing, and used to design and analyze a proportional-integral controller, which targets a specific spanwise wavenumber of the disturbance. Attention is directed towards a quasi-steady case in which the controller update is slower than the convective time scale. This choice enables addressing issues pertinent to sensing, actuation, and control strategy that are also relevant to the control of unsteady disturbances but without the full complexity of transient effects. The feedback controller and plasma actuators perform well, attenuating the streamwise streaks both in the vicinity of the sensors and farther downstream. The controller remains effective for a range of off-design flow conditions, such as when the free-stream velocity is varied. © 2014 AIP Publishing LLC. [<http://dx.doi.org/10.1063/1.4863178>]

I. INTRODUCTION

The relevant underlying mechanism causing boundary layer transition depends on several factors such as the level of free-stream turbulence and surface roughness. In cases where the disturbance level from the environment or the flow boundary is low, a *classical* transition pathway is followed, which is characterized by two-dimensional, exponentially growing, Tollmien-Schlichting (TS) waves followed by secondary instabilities leading to turbulence. At higher disturbance levels, yet not so high as to make nonlinear instability effects important, transition is initiated with the formation of streamwise-elongated structures, called streaks, through a linear transient growth process. The growth of these streaks leads to the establishment of three-dimensional structures and the formation of turbulent spots, bypassing the classical transition pathway and resulting in transition at sub-critical Reynolds number. Further details on transition may be found in the review on boundary layer transition by Saric, Reed, and Kerschen.¹ Regardless of the pathway, the final turbulent state is associated with enhanced mixing and leads to higher stress on, and heat transfer from, the wall. The focus of this study is on the development and implementation of a feedback control system to attenuate the boundary layer streaks that initiate bypass transition.

^{a)} Author to whom correspondence should be addressed. Electronic mail: lavoie@utias.utoronto.ca.

In recent years, there has been substantial progress in the use of modern, model-based, linear, feedback control theory in computational feedback flow control studies,² which has been shown to significantly outperform classical proportional control schemes.³ Notably, Högberg and Henningson⁴ applied linear optimal control theory to boundary layer transition (both TS and bypass). They, as well as several others, provide benchmark data for the potential benefit of modern control techniques. However, bridging the gap between the successful control strategies in computational studies that have access to full flow field information and experiments with only limited sensing and actuation is crucial. In addition, reducing the order of the model used to represent the boundary layer dynamics renders the computational cost of the control tractable, which is essential for realtime control implementation. This is possible by capturing the essential input-output dynamics of the flow (for example, Refs. 5 and 6). In addition, effective positioning of limited number of sensors and actuators depends on the flow and the particular type of sensor and actuator.⁶

Experimental boundary-layer control demonstrations are rare and their outcomes are typically less impressive compared to simulations. Kerho *et al.*⁷ used a reactive control system to target low-speed streaks in a turbulent boundary layer (TBL) with suction at the wall. A 26% decrease in skin friction for continuous suction, with reduced levels using the reactive controller, was inferred from momentum thickness measurements. Rathnasingham and Breuer⁸ used a linear controller based on stochastically estimated transfer functions between the inputs and outputs in a TBL. The feedback/feedforward control led to 7% reduction of mean wall shear stress measurements, which was inferred from the measured velocity profiles using the Clauser chart method. Jacobson and Reynolds⁹ demonstrated some success in countering the disturbance produced by a stationary vortex pair embedded in a laminar boundary layer using a synthetic-jet actuator that forms a counter-rotating vortex pair of opposite sign to that introduced into the boundary layer. Lundell¹⁰ employed distributed suction with upstream sensing to target the streaks occurring in a laminar boundary layer caused by free-stream turbulence. Lundell showed attenuation of the low-speed streaks and the inhibition of their growth for up to 40 boundary layer thicknesses using a region of actuation extending approximately 18 boundary layer thicknesses along the span. Later, Lundell, Monokrousos, and Brandt¹¹ demonstrated that transition delay may be possible by extending the control region across the entire span of the boundary layer using a numerical simulation matched with the aforementioned experiments. This work also demonstrated the practical utility of system identification for higher controller efficiency over the *ad-hoc* threshold and delay control method applied experimentally. Furthermore, Lundell, Monokrousos, and Brandt¹¹ highlighted the difficulty associated with the suction actuation applied by solenoid valve arrangements and suggested that significant efforts should be directed at the development of durable, flexible, small, and inexpensive actuators.

The effectiveness of control systems is inherently linked to the ability of the actuator to alter the flow to a desired state. Therefore, actuators are a critical enabling technology component in any active flow control system. Single-dielectric-barrier-discharge (SDBD) plasma actuators, herein referred to as plasma actuators, offer several major practical advantages: they have no moving parts, can be flush-mounted to the wall, and are relatively easy and inexpensive to construct. Plasma actuators have recently been used to attenuate TS waves in a laminar boundary layer under an adverse pressure gradient.¹² In this case, the actuator forcing was in the streamwise direction. When two actuators are implemented such that they cause opposite forces in the spanwise direction of the flow, a streamwise vortex pair is generated. Arrays of such actuator pairs can be used, for instance, to induce transition¹³ or to maintain attached flow.^{14–16} Other configurations have been applied for alternating spanwise forcing in a turbulent boundary layer,¹⁷ or for jet vectoring.¹⁸ The basic operating principle for all these examples is the weakly ionized region of air produced by the actuator (termed plasma), experiences a Lorentz force by an electric field resulting in a force on the surrounding fluid, which is exploited for flow control purposes. Corke, Post, and Orlov¹⁹ and Moreau²⁰ provide in-depth reviews of the operation, physics, and application of these actuators.

Recently, Hanson *et al.*²¹ used a spanwise array of plasma actuators to successfully control transient growth modes in a Blasius boundary layer. The actuators were arranged to generate streamwise oriented, counter-rotating vortices, similar to those of Ref. 13, but with very small actuator output, such that streaks of comparable amplitude, but opposite sign, of the targeted disturbance were generated. It was also shown that the control effectiveness could be greatly affected by the actuator

array geometry, which influences the distribution of the modal content of the resulting disturbance. For all actuators employed, a high level of control over the targeted spanwise wavenumber was maintained; typically resulting in over 95% reduction of the energy of the corresponding mode. Later, it was shown that the driving frequency and voltage of the actuator also influences the distribution of the modal content of the resulting disturbance.^{22,23}

The objective of this study is to implement a feedback controller to inhibit the transient growth of streaks in a Blasius boundary layer. The control objective is to minimize the disturbance by reducing the energy in the single spanwise wavenumber corresponding to the spanwise spacing of the streaks, as measured by the wall shear stress sensors. The methodology invoked is to embed streaks in the boundary layer at known locations using a spanwise array of cylindrical roughness elements.^{24–27} This provides a tractable model problem in which to determine the effectiveness of the control system prior to the more complex case having a stochastic forcing environment provided by free-stream turbulence. In this work, a novel monotonic control objective is used as part of an empirical model of the flow's response to forcing. This model is used to design and analyze a proportional-integral controller.

The effectiveness of the feedback controller is studied for both a steady and slowly time varying disturbance (i.e., where the time scale of variation is much larger than the convective time scale). Although transient flow effects are not addressed, issues are highlighted that have not been examined previously and are equally critical for control at faster time scales. These include aliasing in feedback sensing in control of individual spatial Fourier modes in the measurements (due to the limited number of sensors usable in practice), the confinement of feedback to near-wall measurements, which provides limited information about the flow farther from the wall (full-state feedback), plasma actuator nonlinearity when operated at the very low voltage levels necessary for transition control, and off-design performance of empirical input-output models.

Our focus on laminar boundary layer control is motivated by the inherent larger spatial and temporal scales compared to the turbulent case, making the laminar boundary layer problem more tractable for the experimentalist.²⁸ However, there is evidence that the sub-layer streaks occurring in a turbulent boundary layer and those occurring in bypass transition are governed by the same linear mechanism.²⁹ Therefore, this work is a step toward the more complex demonstration of wall-bounded turbulence control.

II. EXPERIMENTAL DETAILS

Measurements were made in the closed-loop wind tunnel at the University of Toronto Institute for Aerospace Studies, for which the working section is 1.2 m × 0.8 m and 5 m long. Adjustable fillets located in the corners of the test section allow adjustment of the pressure gradient. The free-stream turbulence intensity was less than 0.05% at $U_\infty = 5$ m/s, the average free-stream velocity used in the present experiments. A baseline laminar boundary layer was established on a cast aluminum plate, 2.1 m long, 12.7 mm thick, and spanning the 1.2 m width of the test section. The plate was mounted 0.23 m above the floor of the test section, which was between 1/4 and 1/3 of the test-section height to minimize potential effects of secondary flows.³⁰ A machined aluminum insert was flush mounted with the cast-aluminum plate. This insert held the roughness element assembly and the removable sensor/actuator assembly. The boundary layer plate was equipped with an asymmetric leading edge geometry, which was designed to minimize the adverse pressure gradient at the leading edge and extent of the region over which it is observed (see Hanson, Buckley, and Lavoie³¹). The location of the stagnation line was controlled using a 0.4 m long flap at the downstream end of the test plate. A schematic of the boundary layer plate is shown in Figure 1.

Measurements of the streamwise flow velocity (U) were made by two Auspex single hot-wire boundary layer probes. Each probe was comprised of a 5 μ m diameter copper-plated tungsten wire with an active length of approximately 1 mm. The hot-wire probes were operated using a constant temperature anemometer with an overheat ratio of 1.5. The hot-wires were calibrated against a pitot-static tube connected to a MKS Model 223, 0–1 Torr, pressure transducer. King's law was fitted to 16 calibration velocities between $0.2U_\infty$ and $1.25U_\infty$. Each velocity measurement consisted of an average of 5 s of data, which passed through an analog low-pass filter with a cut-off frequency

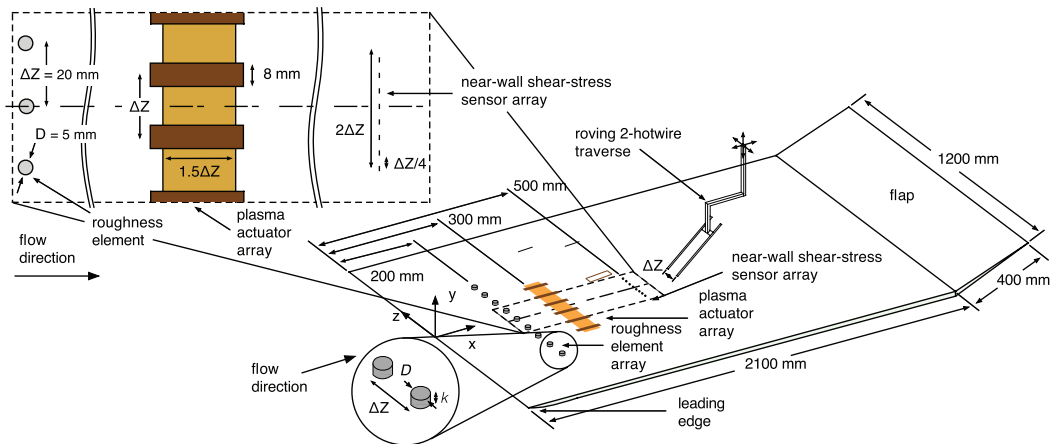


FIG. 1. Schematic of the experimental arrangement with a detailed view of the control region.

of 2.1 kHz, and then sampled at 5 kHz with a 16-bit National Instruments PCI-6259, A/D data acquisition card, connected to a PC. Temperature corrections were applied to the hot-wire data³² using measurements from a T-type thermocouple located in the freestream to account for the ambient temperature variation, which remained within $\pm 0.5^\circ\text{C}$. Calibrations of the hot-wires were performed immediately before and after each experiment to quantify the drift of the hot-wires over the time of the experiment. The total uncertainty of the velocity measurements was estimated to be within $\pm 1.1\%$. Errors were calculated using standard uncertainty analysis methodologies, see, for example, Moffat³³ and Taylor.³⁴

The two hot-wire probes were separated by 20 mm in the spanwise direction. They were positioned locally at the same wall-normal and streamwise coordinate using a custom built mount with an integrated 3-axis Newark micro-stage. The hot-wire probes were then positioned globally using a computer-controlled 3-axis traversing system, which was driven by stepper motors. The resolution of this system was at least $2.5\ \mu\text{m}$ and the minimum precision of the traverse, based on the lead screw accuracy, was $\pm 1\ \mu\text{m}$ over a span of 10 mm. Each velocity profile consisted of measurements of the streamwise velocity at 45 wall-normal locations over a region extending into the freestream. The first wall-normal position of the hot-wire was located using a program that searched for a mean velocity less than 20% of U_∞ . The geometric location of the wall was evaluated by a linear fit to the measurements points between 20% and 35% of U_∞ and extrapolating to determine the offset location where the mean local velocity $\langle U \rangle_t$ was zero, where $\langle \cdot \rangle_t$ represents the time average.

A. Base flow

The baseline laminar boundary layer was measured at $U_\infty = 5\ \text{m/s}$ with the roughness element array retracted flush to the surface of the boundary-layer plate and with the actuators off. These measurements agree well with the Blasius solution, which is illustrated in Figure 2(a) for a typical velocity profile. The location of the virtual leading edge ($\hat{x} = 0$) is located 21 mm downstream of the geometric leading edge location ($x = 0$), which was determined from measurements of the displacement thickness³⁰ shown in Figure 2(b). The laminar boundary layer closely followed a zero-pressure gradient. This was verified quantitatively by the shape factor, $H_{12} = \delta^*/\theta$, where δ^* is the displacement thickness and θ is the momentum thickness. As shown in Figure 2(c), the shape factor remained near the Blasius value of 2.59 over the measurement region of the plate.

The disturbance targeted by the control was generated by an array of cylindrical roughness elements. These arrays have been shown to cause transient growth of streamwise oriented streaks of spanwise-periodic low and high streamwise velocity in the laminar boundary layer,^{24–26} which adequately simulates the bypass transition phenomena. The array consists of nine cylindrical roughness

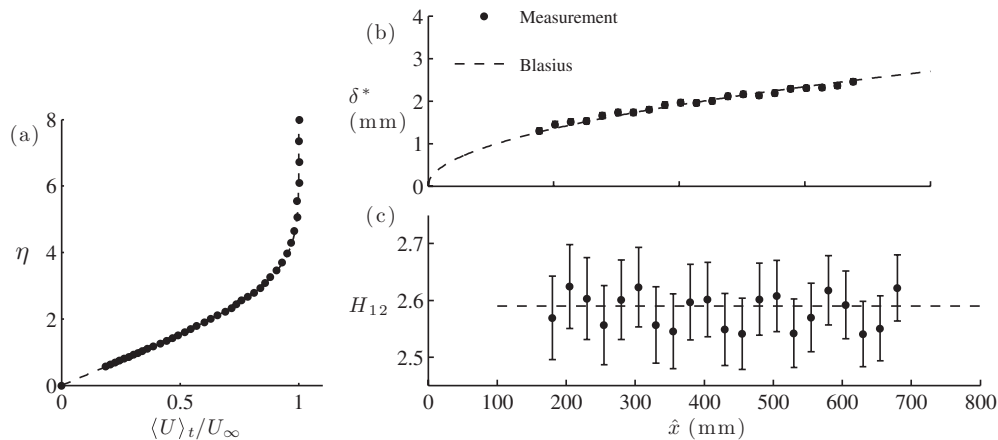


FIG. 2. (a) Comparison of a measured boundary layer profile, \bullet , with the Blasius solution, $---$. (b) Comparison of the measured displacement thickness with the Blasius solution. (c) Streamwise variation of the shape factor, H_{12} . The dashed line corresponds to the Blasius solution, $H_{12} = 2.59$.

elements of diameter $D = 5$ mm, located 200 mm downstream of the physical leading edge of the test plate. The height of the roughness element array was adjusted from a wall-flush position ($k = 0$) to a maximum height of $k = 1.75$ mm. The inter-element spacing was $\Delta z = 20$ mm along the span. The roughness elements were located in an insert that fit flush into the plate. For the present results, the Reynolds number based on roughness deployment height, $Re_k = U_k k / \nu$, was between 84 and 418, where U_k is the mean velocity of the boundary layer at height k with the roughness elements withdrawn, at the x location of the roughness elements.

B. Control system elements

1. Plasma actuator

The upstream edge of the plasma actuator array was located 300 mm downstream of the plate's leading edge as shown in Figure 1. The actuator tile consisted of 1 μm thick copper electrodes deposited on a 0.2 mm thick borosilicate glass dielectric layer as shown in Figure 3. The manufacturing method of these actuators is outlined in Houser *et al.*³⁵ Two of the 60 mm square actuator tiles, each with three surface mounted high voltage (HV) electrodes, were placed side-by-side to produce a spanwise plasma actuator array with six evenly spaced HV electrodes, as shown in Figure 1. The grounded electrode spanned the width of the actuator tile, and extended 30 mm in the

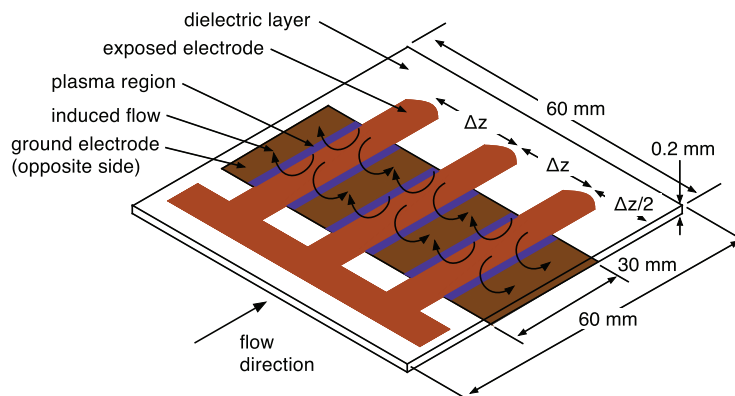


FIG. 3. Schematic of a spanwise plasma actuator tile.

streamwise direction. The HV electrodes were spaced 20 mm apart (matching the spanwise spacing of the roughness, Δz), and their width was 8 mm. The width and spacing of the exposed electrodes was based on the design by Hanson *et al.*,²¹ utilizing the design that caused the highest total energy attenuation of streaks. The actuator was fit into the removable sensor/actuator insert, flush with the surface, which was situated in the boundary layer plate.

2. Wall-shear-stress sensors

Wall-mounted hot-wire sensors were used to measure the streamwise shear stress to provide feedback of the “flow state.” These sensors provide a spanwise-distributed measurement of the streamwise wall shear stress, which is altered by the presence of the streaks.³⁶ The streamwise shear stress data were acquired using an array of eight near-wall mounted hot-wire sensors, which were distributed uniformly along the span with $\Delta z/4$ inter-sensor spacing at $x = 500$ mm. This arrangement provided four measurement locations per fundamental disturbance wavelength (Δz). Therefore, the Nyquist wavenumber corresponds to a wavelength of $\Delta z/2$ and the presence of modes higher than the first harmonic of the fundamental will produce aliasing (this issue is examined in Sec. IV B). The sensors were arranged such that the first sensor was located at $z/\Delta z = -1$ and the fifth sensor was located at $z/\Delta z = 0$, which were both directly downstream of a roughness element.

The shear stress sensor array was constructed onto a 65 mm-by-20 mm plug that was flush-fit into the flat plate. A schematic of the plug and sensor arrangement is shown in Figure 4. The plug was fabricated from electrical-grade fiberglass and fitted with eight pairs of stainless-steel supports. Each hot-wire, which had a sensing element with the same geometry as described previously for the roving hot-wires, was mounted across a pair of the support prongs (0.127 mm diameter jewellers broaches) protruding 1 mm from the plug surface. This placed each hot-wire within the linear region of the Blasius velocity profile for calibration against the Blasius wall shear stress.

The wall mounted hot-wires were operated by constant temperature anemometers, following the same procedures previously outlined. The calibration methodology for wall-mounted hot-wire measurements of shear stress is well established.^{30,37,38} The relationship between the wall-mounted hot-wire voltage and shear stress was determined using the free-stream velocity directly above the sensors, together with the analytical relationship for wall shear stress in a Blasius boundary layer, which was empirically verified (see Figure 2), *viz.*,

$$\tau = 0.332\rho U_\infty^2 Re_x^{-1/2}, \quad (1)$$

where Re_x is the Reynolds number based on the virtual boundary layer origin. A 14-point King’s law fit, provided a suitable relationship for the required measurements over a free-stream velocity $U_\infty \pm 0.5U_\infty$.³⁷

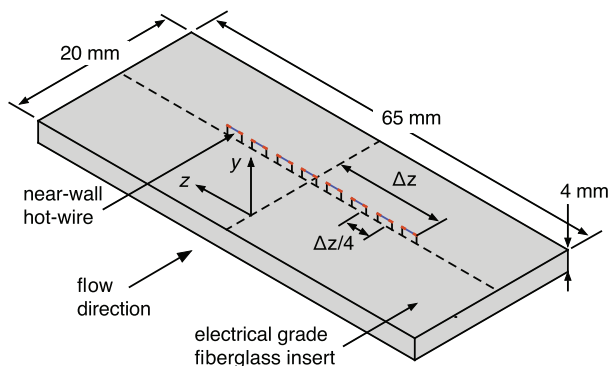


FIG. 4. Schematic of the shear-stress sensor array plug.

C. Control system hardware

The hardware used to implement the control system is operated discretely in time. The analog voltage signals from the wall-shear-stress sensor array were digitized by the data acquisition system described in Sec. II. The digitized information was averaged over 0.05 s to filter high frequency noise and fed to the controller, which computes the actuator input voltage. The latter was fed to an Agilent 32210A waveform generator via a VISA-USB interface to the PC, and the output of the function generator was amplified by a TREK Model 20/20C high voltage amplifier, which was connected to the array of plasma actuators. The total time required for each iteration of the controller using this system is 0.5 s.

III. EMPIRICAL MODEL AND CONTROLLER DESIGN

The control objective is to cancel the growth of streamwise streaks, with a spanwise wavelength of Δz , triggered by the roughness elements by generating counteracting structures with the plasma actuator array. Thus, the experimental arrangement has two types of inputs, as shown in Figure 1, which are caused by the array of roughness elements and the plasma actuators. The output is based on the shear stress measurements. In this section, an empirical input-output model of the system is defined, which is then used to design a controller.

Herein, the non-dimensional wavenumber, $\beta_i = 2\pi \delta i / \Delta z (i = 1, 2, \dots)$, is used to refer to the Fourier component of the streaks signature with a spanwise wavelength of $\Delta z / i$, where $\delta = \sqrt{\nu \hat{x} / U_\infty}$ is the Blasius similarity length scale. For example, the β_1 -mode corresponds to the component of the streaky structure having a wavelength of Δz . At the streamwise location of the shear stress sensors, β_1 is approximately 0.4.

A. Choice of the output

Ideally, it is desirable to provide feedback information by measuring the high and low velocity within the boundary layer. This would require embedding an array of velocity sensors within the flow, which would produce unacceptable interference with the flow. Therefore, in the present work the output is provided from a spanwise array of streamwise-wall-shear-stress sensors (placed at one streamwise location).

Since the goal is to cancel the β_1 -mode streaky structures, only this Fourier component of the spanwise variation of the velocity that corresponds to the disturbance is of interest. Further, the plasma actuator array creates a β_1 -mode with a fixed spanwise phase, so the corresponding roughness-generated streaks can only be affected at this fixed phase. With all of this in mind, a suitable output for the model would be the β_1 -mode of the velocity which has the same phase as the controller, which we call “projected velocity,” φ_{CU} . However, such velocity measurements are not available as the controller is running; only shear stress measurements are available. Thus, we use an analogous quantity, the projected shear $\varphi_{C\tau}$, and find that it is proportional to φ_{CU} (as described in the discussion of Figure 7 below).

An example of the disturbance caused by the array of roughness elements is shown in Figure 5 over a cross-flow (y - z) plane. The y - z plane was located 10 mm upstream of the shear stress sensors, at $x = 500$ mm, to prevent potential damage by the roving hot-wires. Thus, the results are representative of the disturbance found in the “control plane”; i.e., that above the wall-shear sensor array. Two sample contour plots of the disturbance velocity are shown in Figure 5 for the roughness element array deployed to (a) $k = 1$ mm and (b) $k = 1.5$ mm. The disturbance velocity is defined as $U' = \langle U \rangle_t - \langle U \rangle_{tz}$, where $\langle U \rangle_t$ is the time-averaged velocity and $\langle U \rangle_{tz}$ is the spanwise average of $\langle U \rangle_t$. As seen from Figure 5, high-speed streaks are centred about $z/\Delta z = -1, 0, \text{ and } 1$, which correspond to spanwise locations of the roughness elements, while the low-speed streaks are centered about $z/\Delta z = -0.5 \text{ and } 0.5$. This result is typical for all k values considered in this study and similar results have been shown by Fransson and Brandt.²⁵

At the off-wall location of the shear stress sensors, $\eta \approx 0.85$, the spanwise profile of the streamwise disturbance velocity is shown for each case in Figures 5(c) and 5(d), using black circles.

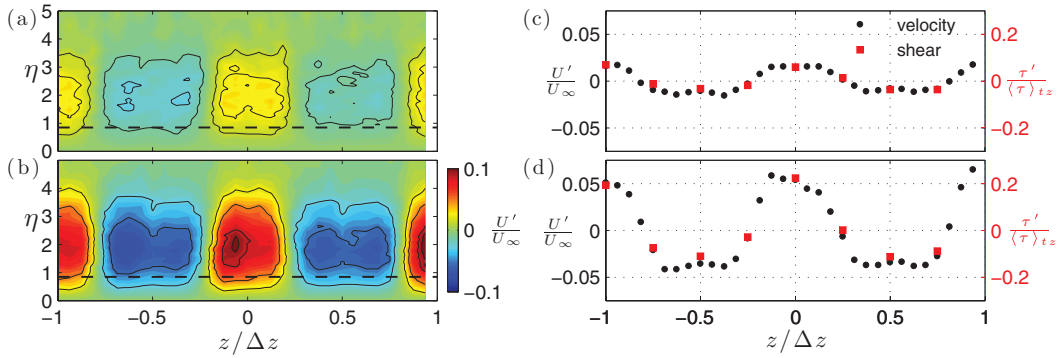


FIG. 5. Contour plots of the streamwise velocity disturbance for (a) $k = 1$ mm and (b) $k = 1.5$ mm. Spanwise profile of the disturbance velocity at $\eta = 0.85$, and disturbance shear stress for (c) $k = 1$ mm, and (d) $k = 1.5$ mm.

Measurements of the normalized disturbance shear stress are overlaid on the disturbance velocity plots, using red squares. The disturbance shear stress is defined as $\tau' = \langle \tau \rangle_t - \langle \tau \rangle_{tz}$, where, again, $\langle \cdot \rangle$ denotes an average with respect to the dimensions in the subscript. As shown in Figures 5(c) and 5(d), the disturbance shear stress tracks the disturbance velocity measurement, albeit with lower spanwise resolution.

At the same y - z plane we find the effect of the plasma actuator alone. The velocity disturbance profiles for two sample conditions, $V_{pp} = 3.9$ and 5.1 kV, are shown in Figures 6(a) and 6(b), respectively (where the voltage is the peak-to-peak voltage (V_{pp}) of the waveform employed to drive the actuators). In comparison to the roughness-induced disturbance, the effect of the actuator is comprised of a higher-mode energy, which has been shown to cause the double-peaked contour shape within the low- and high-speed streaks in Figure 6.²¹ Since the actuator is located farther downstream than the roughness element array, higher modes introduced by the actuator into the flow have less streamwise distance to decay before reaching the downstream measurement plane.

The output, $\varphi_{C\tau}$, is defined mathematically as follows. The disturbance shear stress (τ') measurements are normalized by their corresponding average shear stress, $\langle \tau \rangle_{tz}$, which is roughly equal to the undisturbed laminar shear stress, and are Fourier transformed, with respect to z . The coefficient of the β_1 -mode (with spanwise wavelength of Δz) is denoted by $\tilde{\tau}'_{\Delta z}$. Similarly, the Fourier coefficient for the corresponding mode of the disturbance velocity is $\langle \tilde{U}'_{\Delta z} \rangle_y$, which is obtained from an average of $\tilde{U}'_{\Delta z}$ over the wall-normal direction to result in a single complex number. $\tilde{\tau}'_{\Delta z}$ and $\langle \tilde{U}'_{\Delta z} \rangle_y$ physically represent the phase and magnitude of the β_1 -mode for the wall shear stress and velocity, respectively. The phase that can be controlled by the plasma actuators is the angle of the complex number $\langle \tilde{U}'_{\Delta z} \rangle_y$ obtained from data such as that shown in Figure 6, in the absence of roughness disturbance but with the plasma actuator turned on, *viz.*,

$$\tilde{C}_U = \frac{\langle \tilde{U}'_{\Delta z} \rangle_y}{\| \langle \tilde{U}'_{\Delta z} \rangle_y \|}, \quad (2)$$

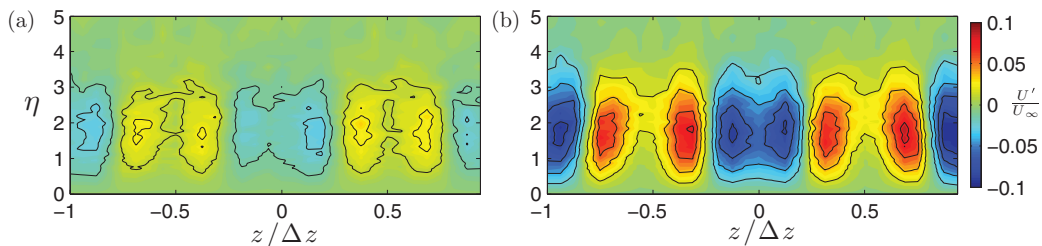


FIG. 6. Contour plots of U'/U_∞ for the plasma actuator with (a) $V_{pp} = 3.9$ kV and (b) 5.1 kV.

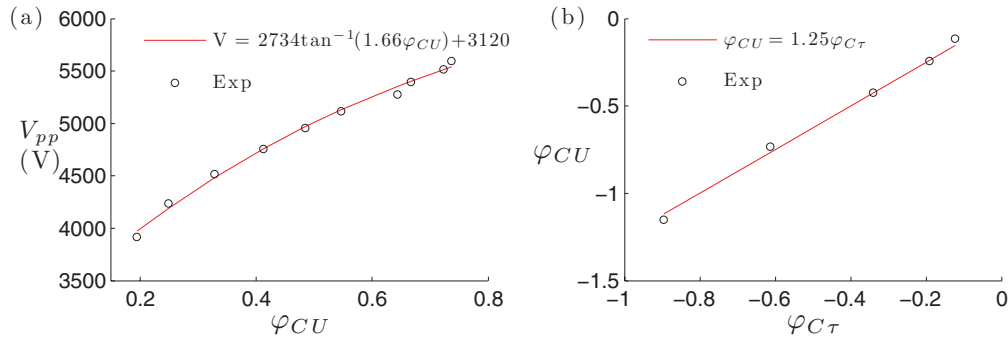


FIG. 7. (a) Relationship between the actuator voltage and projected velocity with the inverse tangent fit. (b) The linear relationship between the projected velocity and shear for the disturbance caused by the roughness element array.

which is nearly identical to the corresponding phase of $\tilde{\tau}'_{\Delta z}$. Considering complex numbers as two-dimensional vectors, we define the output (or projected shear), $\varphi_{C\tau}$, as a dot product, *viz.*,

$$\text{output} = \varphi_{C\tau} = \text{dot}(\tilde{C}_U, \tilde{\tau}'_{\Delta z}) = \text{real}(\tilde{C}_U) \cdot \text{real}(\tilde{\tau}'_{\Delta z}) + \text{imag}(\tilde{C}_U) \cdot \text{imag}(\tilde{\tau}'_{\Delta z}). \quad (3)$$

A similar quantity, projected velocity, is defined as

$$\varphi_{CU} = \text{dot}(\tilde{C}_U, \langle \tilde{U}'_{\Delta z} \rangle_y). \quad (4)$$

Due to the spanwise arrangement of the roughness elements relative to the plasma actuators, the β_1 -mode caused by only the roughness element array will have a negative value of $\varphi_{C\tau}$ and φ_{CU} , whereas the one caused only by the plasma actuators will be positive. The goal of the controller is to drive $\varphi_{C\tau}$ to as small a value as possible (i.e., as close to zero as possible).

This choice of output, $\varphi_{C\tau}$, is better suited for control purposes than the spanwise wavenumber power spectrum of $\tau_{\Delta z}$, used previously by Hanson *et al.*³⁹ The power spectrum yields information only about the strength of the spanwise sinusoidal shear stress variation without providing an indication of the spatial phase of the disturbance along the span. Therefore, an *ad hoc* treatment was required to detect the direction of adjustment of the controller output in Hanson *et al.*³⁹ The underlying issue is that controllers are simpler to design when the output varies monotonically with the input. The output used in this work, $\varphi_{C\tau}$, varies monotonically with the input voltage, as shown in Figure 7.

B. Empirical flow model

Now we find an input-output model from V_{pp} to $\varphi_{C\tau}$ empirically. The response of the boundary layer to forcing by the plasma actuator was measured at 10 operating voltages from 3.9 to 5.6 kV, with a frequency of 1.5 kHz. Below 3.2 kV, the actuator did not cause visible plasma formation and no velocity response was detected; thus, the smallest actuator voltage which was tested, and required during control, was well above the minimum plasma formation voltage. For excitation voltages greater than 3.9 kV, the effect of the actuator increased monotonically with voltage. Unsteady flow was detected for excitation voltages above 5.6 kV, which is indicative of intermittent transition events. The relationship between the actuator voltage input and the *intermediate variable*, projected velocity φ_{CU} , was fit with an inverse tangent function, as shown in Figure 7(a). In practice, any monotonic function which can fit the observed data would have been acceptable for the purposes of the current model. The relationship between the projected velocity, φ_{CU} , and shear, $\varphi_{C\tau}$, was determined from measurements of the disturbance caused by the roughness elements, and found to be approximately linear, as shown in Figure 7(b). The array of roughness elements was deployed from 0.75 to 1.75 mm in increments of 0.25 mm, which had a *similar* range of φ_{CU} as the actuator

case. From these empirical fits, the following relationships were derived:

$$\varphi_{CU} = m \cdot \varphi_{C\tau}, \quad (5a)$$

$$V_{pp} = c_1 \cdot \tan^{-1}(c_2 \cdot \varphi_{CU}) + c_3, \quad (5b)$$

where $m = 1.25$, $c_1 = 2734$, $c_2 = 1.66$, and $c_3 = 3120$. Together, these equations define the relationship between the input V_{pp} and the output $\varphi_{C\tau}$.

C. Control model linearization

The nonlinearity of the \tan^{-1} relationship shown in Figure 7(a) makes it difficult to perform control analysis directly.⁴⁰ Since the form of the nonlinearity is known, the terms were regrouped into a modified plant which takes a new input f , instead of V_{pp} , given by

$$f \equiv \tan\left(\frac{V_{pp} - c_3}{c_1}\right). \quad (6)$$

Equation (5) is then rewritten in terms of f , *viz.*,

$$\varphi_{C\tau} = \frac{f}{m \cdot c_2}, \quad (7)$$

which is a *linear* relationship between the input f and output $\varphi_{C\tau}$. Figure 8 is an illustration of the modified block diagram which takes the input f , and outputs $\varphi_{C\tau}$.

Up to this point, the effect of the roughness elements has been set aside. This effect is now included and assumed to act in the same way as the plasma actuators so that the input to P' is the sum $f + d$. This is a common way to include disturbances for control purposes, and is physically motivated in this case because the plasma actuators are specifically chosen to create the same streak structures as the roughness elements.²¹ The time evolution of the output is given as

$$\varphi_{C\tau}^{i+1} = \frac{f^i + d^i}{c_2 \cdot m}, \quad (8)$$

where i is the discrete time step. The time step corresponds to the time between each control iteration (0.5 s), as discussed in Sec. II C. The left-hand side of (8) is evaluated one time step later than the right-hand side because the measurement is taken one time step after the input is applied. Given a free-stream velocity of 5 m/s, and a distance of 200 mm between the actuators and the shear stress sensors, as shown in Figure 1, the convective time scale is of order 0.04 s. Therefore, the time between control iterations is so long such that the system (boundary layer with applied disturbance and controlled input) comes to equilibrium between discrete time steps. The controlled system dynamics can be expressed in discrete-time state-space form with one state, *viz.*,

$$\begin{aligned} x_{P'}^{i+1} &= 0 \cdot x_{P'}^i + \frac{f^i + d^i}{m \cdot c_2} \\ \varphi_{C\tau}^i &= x_{P'}^i, \end{aligned} \quad (9)$$

where the state, $x_{P'}$, is only an intermediate variable. Equation (9) is the empirical input-output linear model of the plant, P' , and facilitates the design of a controller, K .

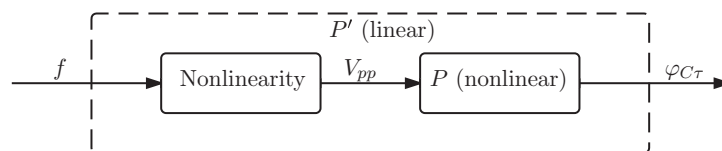


FIG. 8. The linear plant, P' , takes input f , internally converts that via Eq. (6) to V_{pp} , then outputs $\varphi_{C\tau}$ via Eq. (7).

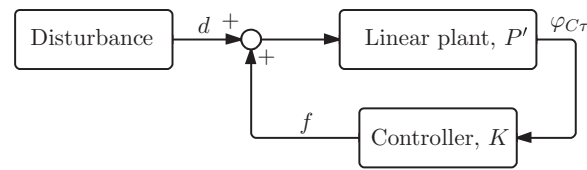


FIG. 9. Block diagram of control scheme with the output defined and a linear plant.

D. PI controller design

In this section, we design a Proportional-Integral (PI) controller for the model given by (9), as depicted in Figure 9. Proportional-Integral-Derivative (PID) controllers are widely used in feedback control for their performance, robustness properties, and simplicity. The integral term ensures that the system can reach the target value, whereas the derivative term typically improves closed-loop stability. A PI controller was chosen for this work since the derivative term is highly sensitive to noise and model uncertainty. Moreover, the plant has only one state, so PI control is equivalent to pole placement.

To choose the PI controller gains, the performance and robustness were analyzed following standard procedures (see, for example, Skogestad and Postlethwaite⁴¹). A measure of performance is how quickly the controller drives $\varphi_{C\tau}$ to zero, whereas robustness is the ability of the controller to perform well in off-design conditions. The controller system, K , evolves as

$$x_K^{i+1} = x_K^i + \varphi_{C\tau}^i, \quad (10)$$

$$f^i = -K_I x_K^i - K_P \varphi_{C\tau}^i, \quad (11)$$

where x_K is the time integral of $\varphi_{C\tau}$ needed for integral feedback. The proportional and integral gains are denoted by K_P and K_I , respectively. The plant and controller systems are combined to yield the state-space equations of the controlled system, *viz.*,

$$\begin{pmatrix} x_{P'}^{i+1} \\ x_K^{i+1} \end{pmatrix} = \begin{bmatrix} \frac{-K_P}{c_2 \cdot m} & \frac{-K_I}{c_2 \cdot m} \\ 1 & 1 \end{bmatrix} \begin{pmatrix} x_{P'}^i \\ x_K^i \end{pmatrix} + \begin{bmatrix} \frac{1}{c_2 \cdot m} \\ 0 \end{bmatrix} d^i, \quad (12)$$

$$\varphi_{C\tau}^i = [1 \quad 0] \begin{pmatrix} x_{P'}^i \\ x_K^i \end{pmatrix}. \quad (13)$$

For the best performance, the state should decay to zero as quickly as possible. For this discrete time system, this implies the eigenvalues of the 2×2 matrix in (12) should be close to zero.⁴¹ It is easily shown that $K_P = K_I = c_2 \cdot m$ makes both eigenvalues zero.

Robustness was considered by the infinity norm of the sensitivity function, $\|S\|_\infty$, which is a measure of robustness to plant model uncertainty (such as would be caused by a change in free-stream velocity), and $\|\cdot\|_\infty$ denotes the infinity norm, defined as the maximum gain over all frequencies. Letting P' and K denote the discrete-time transfer functions of the plant, given by (9), and controller, given by (10)–(11), the sensitivity function is given by

$$S \equiv \frac{1}{1 - P' \cdot K}. \quad (14)$$

A general guideline is for the value of $\|S\|_\infty$ to be in the range of 1.3–2. The contour plots in Figure 10 demonstrate the levels of performance (maximum eigenvalue) and robustness ($\|S\|_\infty$) for a range of PI controller gains. The best performing K_P and K_I (zero eigenvalue) result in $\|S\|_\infty = 2$. For convenience, we define $K_P = K_I = G_c \cdot c_2 \cdot m$, where G_c is the gain coefficient. To accommodate a larger degree of uncertainty in the model of the plant, we choose $G_c = 0.5$, yielding $\|S\|_\infty = 1.33$.

An example of the output, using various values of G_c , is shown in Figure 11. At iteration 0, the system is undisturbed. At the next iteration, a disturbance corresponding with the maximum value considered in the experiments is applied. Control is applied in all subsequent iterations. The

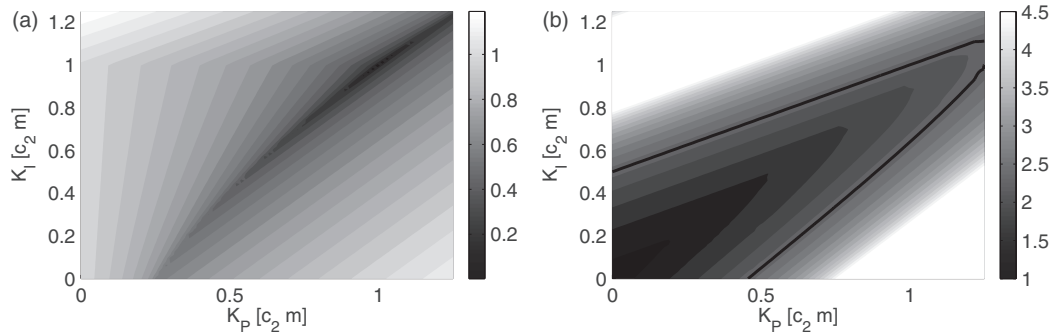


FIG. 10. The maximum eigenvalues of the 2×2 matrix in (12) with control gains (a), and the value of the infinity norm of the sensitivity function (b). The solid line indicates $\|S\|_\infty = 2$.

case with the best performance corresponds with $G_c = 1$. Increasing the gain past $G_c = 1$ results in oscillation of the output, which is typical of an underdamped system. When $G_c = 0.5$, the controller effectively reduces $\varphi_{C\tau}$ to zero after only a few iterations. Further decrease of the gain increases the level of damping.

IV. LIMITATIONS OF WALL SHEAR STRESS SENSORS

The use of discrete sensor locations imposes limits on the effectiveness of the controller. This section overviews the limitations of the shear stress sensors, including comparisons to measurements over the entire thickness of the boundary layer and errors associated with the coarse spacing of sensors along the span.

A. Comparison with measured velocity planes

The shear stress sensors are located 1 mm above the surface as described in Sec. II B 2, corresponding to $\eta = 0.85$ for $U_\infty = 5$ m/s, which increases the signal-to-noise ratio of the measurements relative to sensors placed closer to the wall, while remaining within the range of linear velocity variation with y . However, the feedback signal based on these sensors is only representative of the disturbance in the near-wall region, which may not give accurate information of the disturbance higher in the boundary layer. To examine if this is the case, the energy of the disturbance obtained from velocity measurements at 1 mm above the wall (referred to as “local” below) is compared to that obtained by integrating the energy measured at all heights within the boundary layer. The

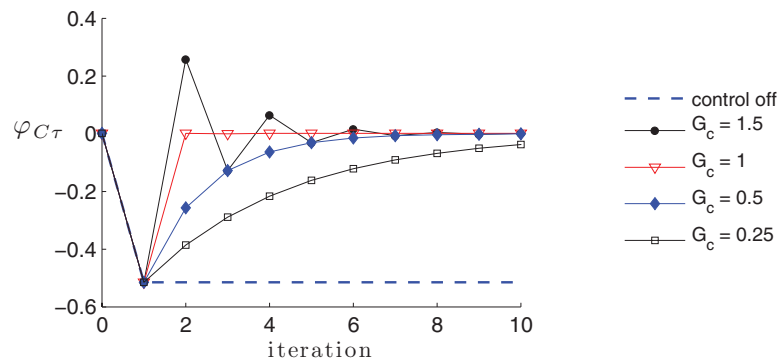


FIG. 11. Output of the feedback controlled model plant (simulated), demonstrating the variation in the response of the PI closed-loop controller to a typical steady disturbance.

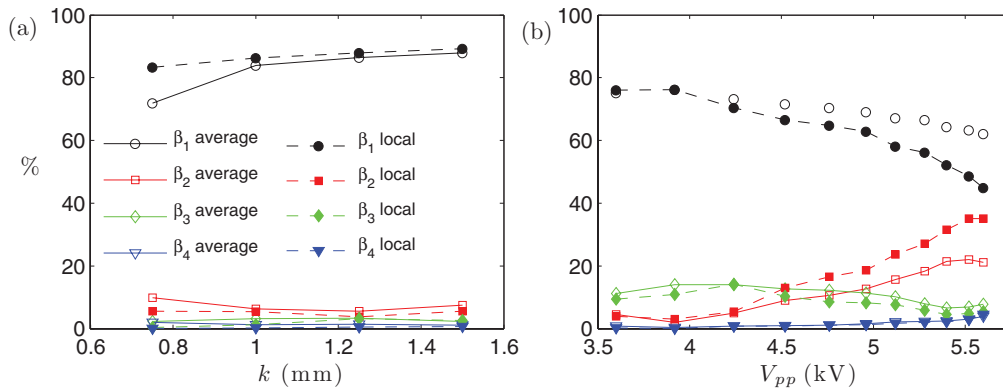


FIG. 12. The variation of the fractional energy contained in β_{1-4} from the near-wall (local) velocity measurements at $\eta = 0.85$, and the boundary layer averaged measurements. (a) For the roughness element array, $k = 0.75$ – 1.75 mm, and (b) for the actuator $V_{pp} = 3.9$ – 5.6 kV.

comparison is done based on the fractional energy content of a given mode, which in the case of local measurements is given by

$$\frac{\phi_{U'}(\beta_i)}{\sum_{i=1}^8 \phi_{U'}(\beta_i)} \times 100\%, \quad (15)$$

where the power spectrum of the disturbance velocity is represented by $\phi_{U'}$. For the boundary-layer-thickness-integrated energy calculation (referred to as “average” below), $\phi_{U'}$ in (15) is replaced by

$$\langle \phi_{U'}(\beta_i) \rangle_y = \frac{\int_0^{5\delta} \phi_{U'}(\beta_i) dy}{5\delta}. \quad (16)$$

The comparison of the local and average fractional energy ratios for β_{1-4} is shown in Figure 12(a) for the roughness array disturbance, and (b) for the actuator. Figures 12(a) and 12(b) show distinctly different trends. As the roughness element deployment height increases, the local and averaged fractional energy ratios reach approximately the same constant value. In contrast, as voltage to the plasma actuators increases, the local and average fractional energy ratios differ. These results imply that at higher voltages the near-wall sensors under predict the boundary-layer averaged energy for the β_1 -mode. These results also suggest a difference in the spatial distribution of the disturbances caused by the roughness and actuator, as shown previously in Figures 5 and 6. Specifically, the effect of the actuator is concentrated nearer the wall, compared to the roughness disturbance. This can be attributed to the reduced streamwise development of the actuated flow, compared to the disturbance caused by the roughness elements, which is introduced upstream of the actuators.

B. Aliasing due to limited spanwise resolution

The goal of this work is to target a spanwise wavenumber of the disturbance having a wavelength Δz . Typically, more than 95% of the average disturbance energy caused by the roughness element array is contained within the first two modes (β_1 and β_2) at the control plane (streamwise location of the shear sensor array). For the plasma actuators, 80% of the average disturbance energy is contained in the first two modes and over 95% of the energy is contained in the first three modes. Due to hardware limitations, we employed four streamwise shear stress measurement locations per Δz wavelength. For this arrangement, the Nyquist wavenumber corresponds to the β_2 -mode. The contribution of higher, unresolved, wavenumbers altered the apparent (i.e., measured) energy of the first two modes. The influence of this aliasing on the shear measurements is found by comparing more densely sampled velocity data (from the roving hot-wire) at the same height above the wall where the shear stress was measured ($\eta = 0.85$).

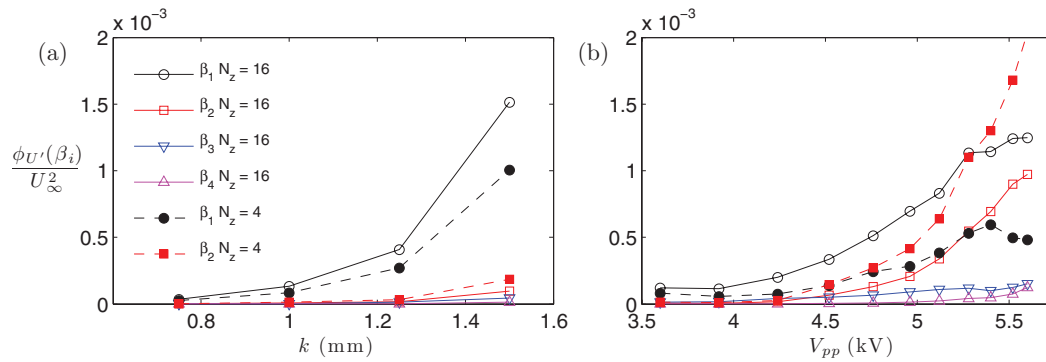


FIG. 13. From $N_z = 16$ velocity measurements over Δz , the energies in the first modes ($\beta_1 - 4$) are plotted and have no aliasing. The energies in $\beta_1 - 2$ are plotted with $N_z = 4$ velocity measurements over Δz , and have aliasing. The flow is disturbed in (a) by roughness elements and actuated in (b) by plasma actuators.

Figure 13 shows the energy contained in the first four modes calculated from down sampling the 16 points per Δz velocity data to 4 points per Δz for the disturbance produced by the roughness element array and actuator. These results are compared against the alias-free modal energy content obtained without down sampling. For the velocity measurements associated with the roughness array (see Figure 13(a)), aliasing was less important than for the actuator array (see Figure 13(b)). As shown by Figure 13(b), significant aliasing occurred due to the increased energy in the unresolved third and fourth modes, compared to the roughness case.

In summary, it is apparent from Secs. IV A and IV B that the actuated flow measured by the shear sensor array will appear as being less energetic than if it had been measured over the entire boundary layer. Aliasing was more significant for the disturbance caused by the actuator owing to a larger content of unresolved energy in the β_3 - and β_4 -modes. The implications of these results are discussed in Sec. V D.

V. EXPERIMENTAL FLOW CONTROL RESULTS

Experimental results on the performance, robustness, and the overall effectiveness of the feedback controller are discussed in this section. First, the effect of control for a steady disturbance input over a range of gain values and free-stream velocities is considered. These include velocity values that differ from the values at which the input-output models are obtained. Next, the performance of the controller to a slowly time-varying input is considered. Key aspects related to the non-modelled characteristics of the system are addressed.

A. Effect of controller gain

The gains of the controller, K_P and K_I , will affect the performance of a closed-loop control system. The condition where $K_P = K_I$ remains near both optimal performance and robustness in Figure 10 for a given controller gain level and is therefore kept equal in this study. Recall from Sec. III D that the gain that would optimize performance was $K_P = K_I = c_2 \cdot m$, yet in this work, the gain was reduced to $K_P = K_I = G_c \cdot c_2 \cdot m$, where $G_c = 0.5$ (the gain coefficient) should be less than unity to increase robustness to uncertainty in the input-output models. Figure 14(a) shows the control results for the cases having a roughness element deployment height of $k = 1.25$ mm, $U_\infty = 5$ m/s, and various G_c values. The figure also contains comparison with results obtained from modelling based on (12) and (13). At time = 0 s, the controller measured the uncontrolled disturbance due to the presence of the upstream roughness element array.

As shown in Figure 14(a), the gain that maximizes the performance (i.e., that resulting in the shortest settling time to reach the controlled state) is $G_c = 1$, corresponding to the best performance case discussed in Sec. III D, where the system is critically damped. Further increase of G_c leads to

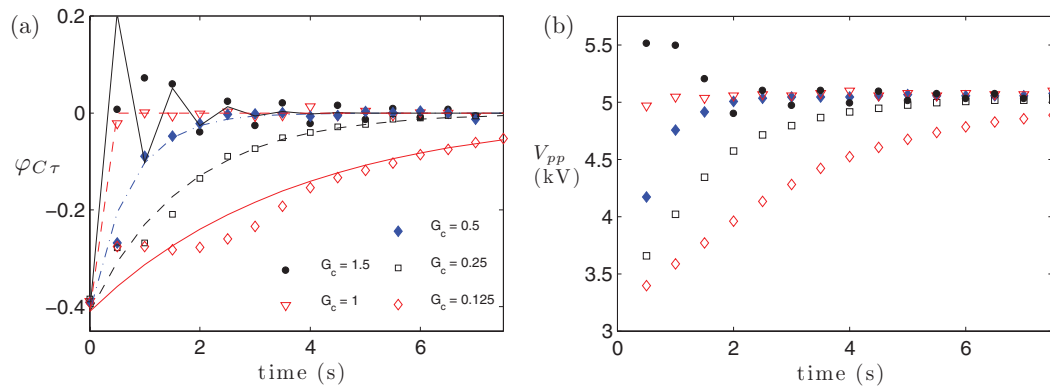


FIG. 14. (a) Dependence of the time variation of the control output $\varphi_{C\tau}$, for $k = 1.25$ mm, $U_\infty = 5.0$ m/s, on G_c . Markers represent the experimental measurements, and lines depict results from the simulations based on (12) and (13). (b) Corresponding plasma actuator voltage.

a damped oscillation of the control response, as shown for $G_c = 1.5$. Lowering the gain leads to an over-damped response, as shown in Figure 14(a), for $G_c < 1$ with reduced performance. It is also noteworthy that the measured data points deviated from the model (lines) for $G_c < 0.5$. This is due to the non-monotonic actuator behaviour at low voltage, which is discussed in the next paragraph.

In Figure 14(b), the actuator voltage is shown for each of the cases examined in Figure 14(a). For $G_c = 0.125$, the first four actuator voltages are below 3.9 kV, which is the lowest voltage used in obtaining the input-output data used for modelling in Sec. III B. After the first iteration (at 0.5 s), an increase in actuator voltage causes stronger control (i.e., closer to zero control output $\varphi_{C\tau}$) than predicted by the model, as seen in Figure 14(a). This is caused by non-monotonic behaviour of the actuator at lower V_{pp} values. This was ascertained by testing at low actuator voltages with the roughness elements retracted (see Figure 15). For voltages less than 3.2 kV, the electric field is insufficient to ionize the air and produce a body force; between 3.2 and 3.8 kV the disturbance at the control plane decreased slightly with increasing voltage. This range of actuator output (frequency and voltage) is not addressed in the open literature. Rather, studies employing plasma actuator for control are focused on plasma actuator output over a wide range of voltage, often at increments of 1 kV or more.

Notwithstanding the non-monotonic actuator behaviour at low voltages, the feedback controlled plant remains stable, as shown in Figure 14(a), since the controller continues to compensate in the correct direction. Feedback provides robustness to this type of non-modelled behaviour; which would destabilize an *ad hoc* controller relying on a less sophisticated objective, as shown by Hanson *et al.*³⁹

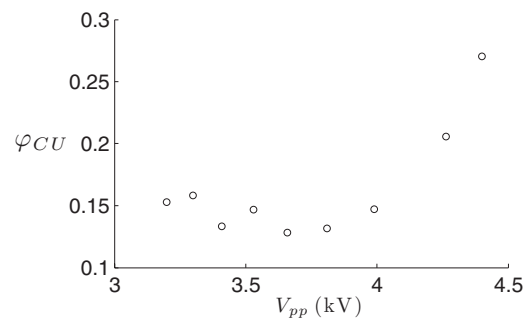


FIG. 15. Variation of φ_{CU} with actuator excitation voltage, depicting non-monotonic behaviour over a range encompassing low voltages: $V_{pp} < 3.9$ kV.

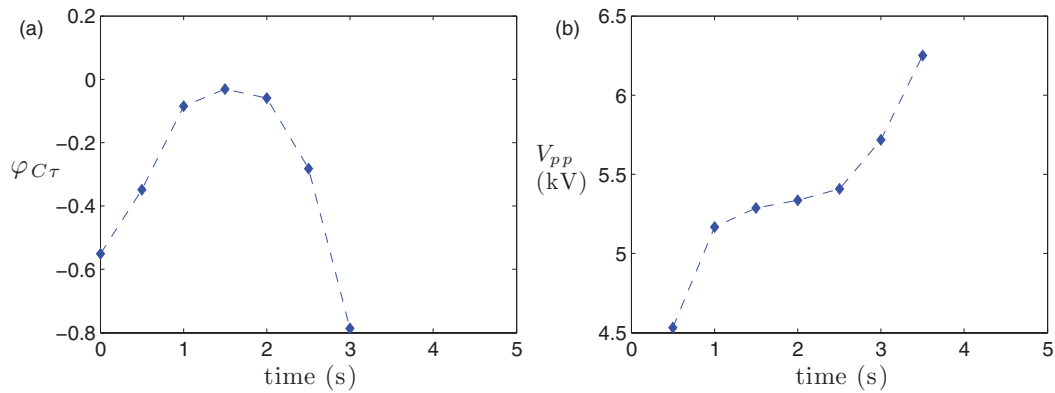


FIG. 16. Evolution of the control objective and input voltage for $k = 1.375$ mm and $U_\infty = 5$ m/s.

B. Effect of aliasing

Results for a second case, with a higher roughness height $k = 1.375$ mm and $U_\infty = 5$ m/s, is shown in Figure 16. The controller gain is set to $K_P = K_I = 0.5 \cdot c_2 \cdot m$, for which successful control is attained at the lower roughness height (Figure 14). For the higher k value, however, the control does not converge, as seen from Figure 16. In this case, the controller attempts to increase the actuator voltage beyond 5.3 kV. As seen from Figure 13(b), for $V_{pp} > 5.3$ kV, in the absence of roughness input, the sensed (wall-shear-based) energy of the β_1 -mode input by the actuator decreases with increasing voltage because of aliasing of the β_3 -mode energy into the β_1 -mode. Consequently, with the presence of roughness disturbance, the measured wall-shear disturbance falsely indicates stronger roughness-induced disturbance with increasing actuator voltage beyond 5.3 kV. The controller compensates by increasing the actuator output (time > 2 s), which results in an unstable control case.

C. Effect of free-stream velocity

Robustness to off-design conditions are tested by exercising the control at free-stream velocities lower than 5 m/s (at which the input-output models were developed). The controller gain in these experiments is $K_P = K_I = 0.5 \cdot c_2 \cdot m$, based on the discussion in Sec. III D. The deployment height of the roughness elements is $k = 1.25$ mm. Free-stream velocities of 3, 3.5, 4, and 5 m/s are considered. Results are shown in Figure 17. At time = 0 s, the controller measured the uncontrolled disturbance due to the presence of the upstream roughness element array.

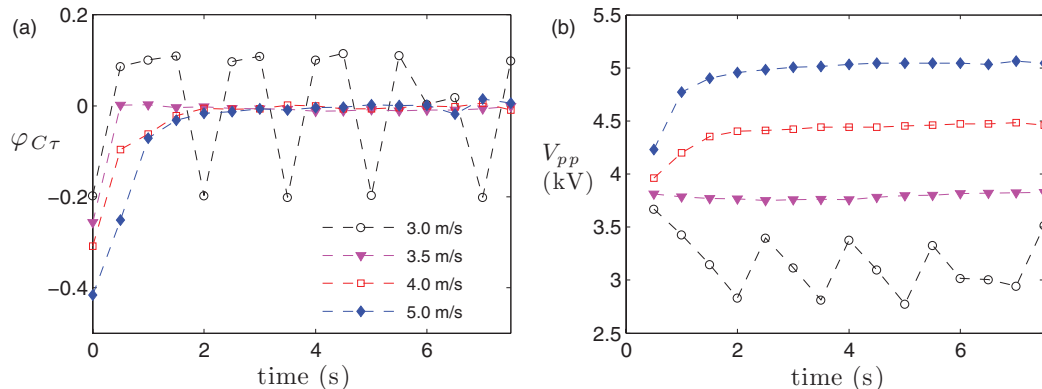


FIG. 17. Influence of varying the free-stream velocity on the control objective and input voltage for $k = 1.25$ mm.

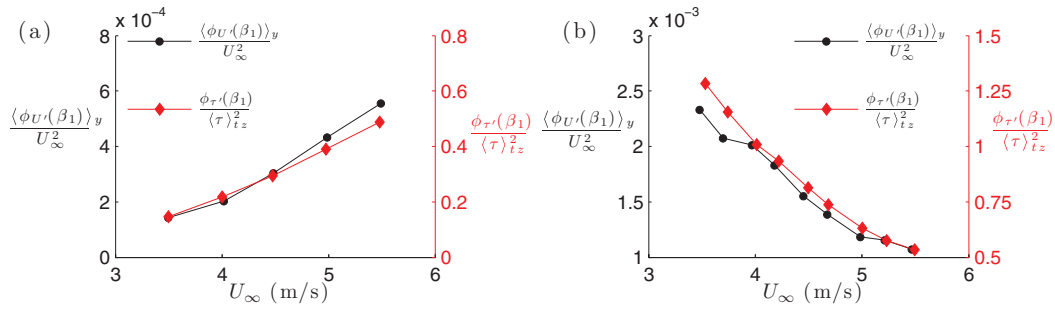


FIG. 18. The energy in β_1 -mode velocity disturbance, as measured over the entire boundary layer, and β_1 -mode wall shear stress as a function of free-stream velocity. The response to roughness elements is shown in (a) and the response to plasma actuators in (b).

Reducing the free-stream velocity lowers the initial uncontrolled plant output and consequently, the required actuation voltage to minimize $\varphi_{C\tau}$. For $k = 1.25$ mm and $U_\infty = 3.5, 4,$ and 5 m/s, $\varphi_{C\tau}$ converges to zero within ± 0.02 (or $\pm 5\%$ of the maximum absolute value of $\varphi_{C\tau}$ at time zero) in less than 2 s, as shown in Figure 17(a). For the case at 3 m/s, the first control iteration results in a high level of actuation and the controller compensates by reducing the actuator voltage. Below 3.6 kV, as shown in Figure 15, a voltage reduction increases the level of forcing at the control plane, which is also shown in Figure 17 for $U_\infty = 3$ m/s during the time window: 0.5–1.5 s (for the first through third control iterations). The controller compensates by reducing the voltage until the actuator output is extinguished ($V_{pp} < 3.2$ kV) and the control objective reaches an uncontrolled value of -0.2 (similar to the initial value). Furthermore, from the empirical model shown in Figure 7, a value of $\varphi_{C\tau} = -0.2$, would correspond to an expected actuation level of 4.5 kV. For free-stream velocities less than the model-development velocity, the actuator voltage required to minimize the control objective is always lower than that predicted by the model.

Increasing the free-stream velocity *increases* the energy of the streaks generated by the roughness elements, but *decreases* the energy of the counter-streaks generated by the plasma actuators. This change in the input-output model response is due to two important physical mechanisms. The first is related to boundary layer receptivity to roughness-induced disturbances and the second to the effect of free-stream velocity on the plasma actuator's control authority. For the roughness element array, as the free-stream velocity increases, so does the velocity at the apex of each element. The thickness of the boundary layer decreases with increasing free-stream velocity and is proportional to $(1/U_\infty)^{0.5}$, which leads to a nonlinear increase in the disturbance velocity and shear stress: this is demonstrated in Figure 18(a) for measurements of the roughness-induced disturbance in the absence of actuation. An *opposite* behaviour is found for the actuator, as shown in Figure 18(b). The actuator delivers a constant power input to the flow over the actuator length for a given voltage. Therefore, an increase in free-stream velocity will decrease the residence time of the fluid over the actuator, which decreases the total energy to a fluid particle. Despite these off-model-calibration changes, the steady state error is driven to zero by the controller due to action of the integral term, see, for example, Figure 17, except for the lowest considered velocity with actuator on/off oscillations.

D. Characterization of the controlled flow

In this section, we examine the effectiveness of the control over the entire boundary layer thickness. Measurements of the velocity disturbance, U' , were again acquired at $x = 490$ mm (effectively the control plane, at $x = 500$ mm, but with a small offset to avoid damaging the wall-shear sensors during velocity probes traversing) for each of the cases considered. An example of the uncontrolled disturbance ($k = 1.25$ mm, $U_\infty = 5$ m/s) caused by the roughness element array is shown in Figure 19(a) and the corresponding controlled flow is shown in Figure 19(b) with $\varphi_{C\tau} \approx 0$ and for the actuator, $V_{pp} = 5$ kV. The corresponding wall-normal energy distributions are shown in Figures 19(c) and 19(d) for the uncontrolled and controlled flow, respectively. The energy in the

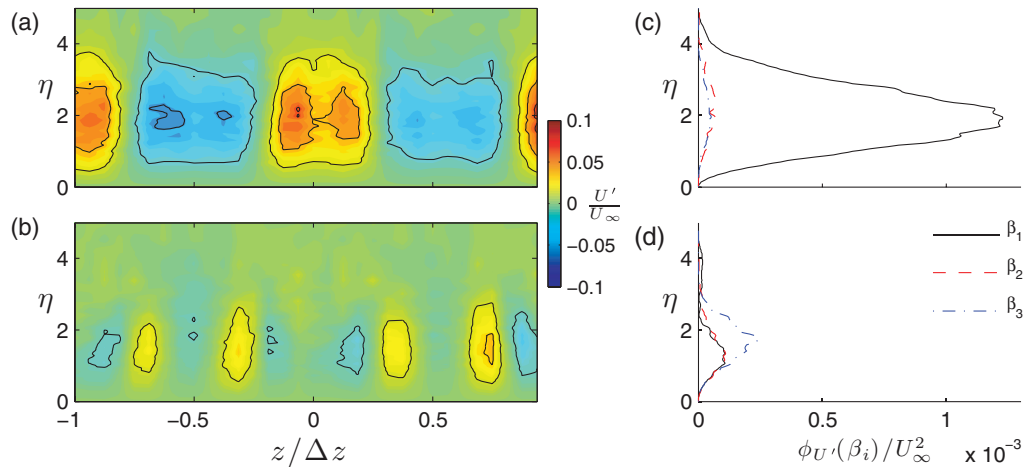


FIG. 19. Contour plots of the disturbance velocity for (a) the uncontrolled flow with $k = 1.25$ mm, and (b) the controlled flow. Wall-normal disturbance energy profiles are shown for the first three modes for (c) the uncontrolled and (d) the controlled flows.

targeted β_1 -mode is substantially reduced. The remaining energy is located predominantly in the lower half of the boundary layer and in the β_3 -mode.

Bandpass spatial filtering of U'/U_∞ for the controlled flow (Figure 19(b)) is used to isolate the β_1 -mode, as shown in Figure 20. Approximately 75% of the residual energy in β_1 -mode with control is contained in the near-wall region, $\eta < 2.5$. The reconstructed β_1 -mode shows that in the near wall region a central low-speed streak is located at $z/\Delta z = 0$, which indicates over-actuation. However, for $\eta > 2.5$ the β_1 -mode has a positive velocity at $z/\Delta z = 0$, which indicates a region of under-actuation.

The cause for this behaviour, over-actuated near-wall region, and under-controlled region of the boundary layer above $\eta = 2.5$, stems from observations made earlier. The measured value of the β_1 -mode energy is too small, and this error is attributed to the effect of aliasing, which was more significant for the actuator than the roughness disturbance, as shown in Figure 13. This results in the near-wall region ($\eta < 2.5$) being over-actuated, despite the control output indicating that the β_1 -mode disturbance is completely attenuated (i.e., $\varphi_{C\tau} \approx 0$). On the other hand, the cause of the β_1 -mode energy occurring above $\eta = 2.5$ is due to a difference in the wall-normal distribution of energy for the roughness array disturbance compared to the actuator case. This difference in wall-normal distribution of the β_1 -mode energy for the roughness disturbance and actuator counter-disturbance is shown in Figure 21. For comparable maximum amplitude β_1 -mode disturbances, the roughness disturbance profiles contain more energy farther from the wall, compared to the actuator disturbance profiles. Thus, the difference between the roughness- and actuator-induced disturbances will always leave a “remainder” disturbance in the upper part of the boundary layer.

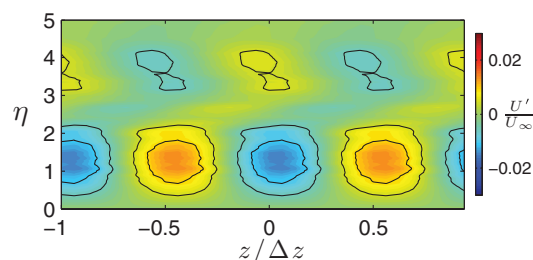


FIG. 20. Contour plot of the β_1 -mode disturbance velocity of the controlled flow.

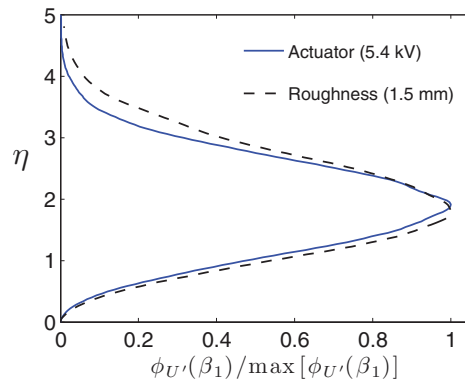


FIG. 21. Wall-normal profiles of the normalized β_1 -mode disturbance caused by the actuator with 5.4 kV and for the disturbance caused by the roughness element array deployed to 1.5 mm.

A comparison of the spanwise-wavenumber power spectrum, averaged over the boundary layer, is shown in Figure 22 for the uncontrolled and controlled flow from the velocity measurements shown in Figures 19(a) and 19(b), respectively. Again, note that the value of β_1 at $x = 490$ mm was approximately 0.4. The remaining energy in the β_1 -mode disturbance is given by

$$\langle \phi_{U'}(\beta_1) \rangle_{yC} / \langle \phi_{U'}(\beta_1) \rangle_{yD} \times 100\%, \quad (17)$$

where the subscript, D , is for measurements of the disturbance only, and C is for measurements of the controlled flow after the controller has converged to a minimal value of the control objective, $\varphi_{C\tau} \approx 0$. For $G_c = 0.5$, this was always achieved before 4 s (or 8 control iterations). For the example shown in Figure 22, approximately 6% of the β_1 -mode energy remains following control attainment. A similar quantification summed over all wavenumbers is given by

$$\sum_{i=1}^8 \langle \phi_{U'}(\beta_i) \rangle_{yC} / \sum_{i=1}^8 \langle \phi_{U'}(\beta_i) \rangle_{yD} \times 100\%. \quad (18)$$

The boundary-layer-averaged energy remaining over all wavenumbers is 26% in this case, which is primarily due to the presence of energy in the β_2 and β_3 -modes not considered by the controller. For all conditions, feedback resulted in a range of 3%–6% of remaining β_1 -mode energy, due to the effects of aliasing, which change with the level of the disturbance and the effect of the actuator at different voltages. Whereas the boundary-layer-averaged energy remaining over all wavenumbers varies from 14% to 26%, due to the presence of $\beta_2 - 4$ -modes not considered by the controller. This range of values follows from the various actuator voltages used for the different control cases, and corresponding changes in the modal composition of the actuator effected flow, see, for example, Figure 12(b).

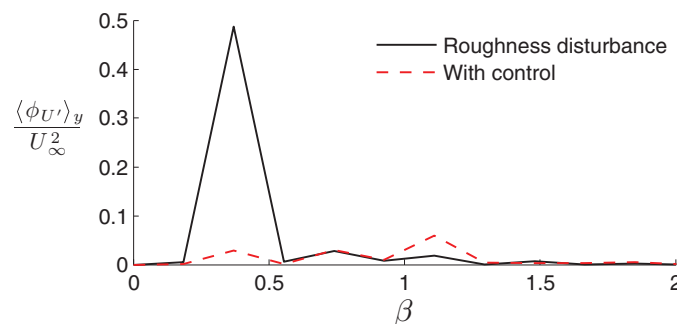


FIG. 22. Average spanwise power spectrum of the disturbance and the controlled flow, from the velocity measurements shown in Figures 19(a) and 19(b), respectively.

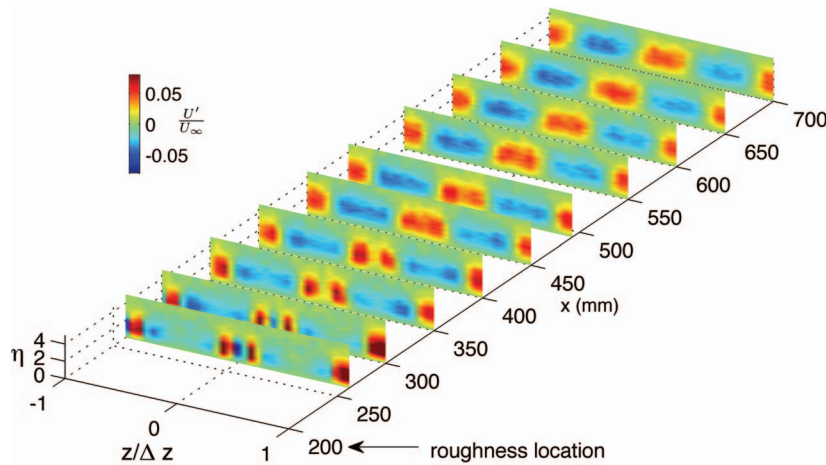


FIG. 23. Streamwise evolution of the disturbance caused by a roughness array with $k = 1.25$ mm and $U_\infty = 5$ m/s.

E. Streamwise evolution of the disturbance and control

In Secs. V A–V D, the control results were presented for only a single measurement plane. In this section, the effect of the control on the transient growth of streaks is examined over multiple streamwise locations. Three cases with different flow conditions are examined. In the first two, the free-stream velocity was 4 and 5 m/s and $k = 1.25$ mm. For the third case, the free-stream velocity was 4 m/s and $k = 1.375$ mm. Measurement planes are at streamwise locations varying from $x = 265$ mm (65 mm downstream of the roughness elements) to $x = 700$ mm, over a spanwise region between $z/\Delta z = \pm 1$, and over the thickness of the boundary layer.

For the case with $U_\infty = 5$ m/s and $k = 1.25$ mm, contour plots of U'/U_∞ for the uncontrolled flow are shown in Figure 23. As the flow developed, higher mode energy decayed, such that the $y-z$ planes past $x = 500$ mm appear to be comprised of primarily a β_1 -mode disturbance, associated with the spacing of the roughness elements. The measurements of the controlled flow are shown in Figure 24. The measurement planes upstream of the plasma actuators are omitted. The controller effectively eliminates the energy in the targeted β_1 -mode, and so it is predominantly higher modes that remain downstream, consistent with the results shown in Figure 19.

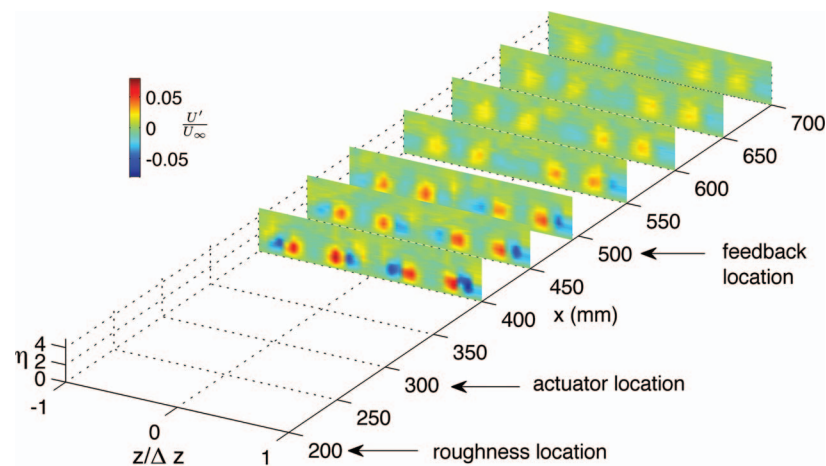


FIG. 24. Streamwise evolution of the flow shown in Figure 23 with control by the plasma actuator operated at 5.05 kV ($\varphi_{C\tau} \approx 0$).

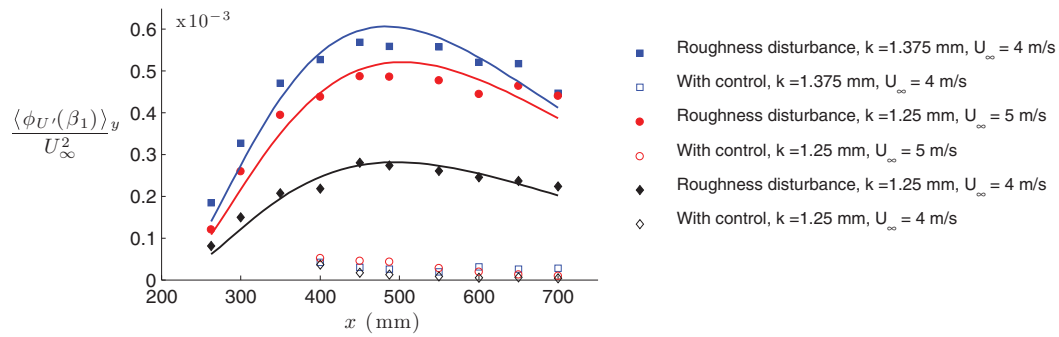


FIG. 25. Disturbance energy evolution of β_1 for $k = 1.375$ mm at 4 m/s and $k = 1.25$ mm at 4 and 5 m/s. Control results have comparable open symbols, and the lines are fit from the function described by White, Rice, and Gökhan Ergin.²⁶

The transient growth (i.e., initial algebraic growth followed by exponential viscous decay) of the disturbance with increasing x for each of the three cases is shown in Figure 25. A function of the form, $\frac{\langle \phi_{U'} \rangle_y}{U_\infty^2} = A(x - x_0)^2 \cdot \exp[-B(x - x_0)]$, where A represents the algebraic growth rate, B^{-1} represents an exponential decay length scale, and x_0 is the distance to the roughness element array location from the leading edge (200 mm), representing the growth and decay of energy is fit to the data points, which follows from the work of White, Rice, and Gökhan Ergin.²⁶ The controlled flow is again quantified by the remaining energy in the β_1 -mode disturbance as given by (17). The variation of remaining energy in the β_1 -mode is shown over $x = 400$ –700 mm, in Figure 26 for each of the three cases shown in Figure 25. Near the control measurement plane, at $x = 490$ mm, the remaining β_1 -mode energy is less than 8% for all cases; however, it is slightly increased upstream of the control measurement plane. Farther downstream, remaining β_1 -mode energy continued to decrease, and corresponds with a region of exponential decay of the disturbance shown in Figure 25 for $x > 500$ mm.

F. Continuous free-stream velocity perturbation

The ability of the controller to track a slowly time-varying disturbance was studied. The free-stream velocity was varied sinusoidally at a period (T_w) of 50 s and an amplitude of 1 m/s between 4 and 5 m/s. The height of the roughness element array was fixed at $k = 1.25$ mm. For comparison, the time scale associated with the streamwise distance between the actuators and feedback sensors (200 mm), and for a convection velocity of 5 m/s, is nearly three orders of magnitude smaller than the slowly time-varying disturbance considered here.

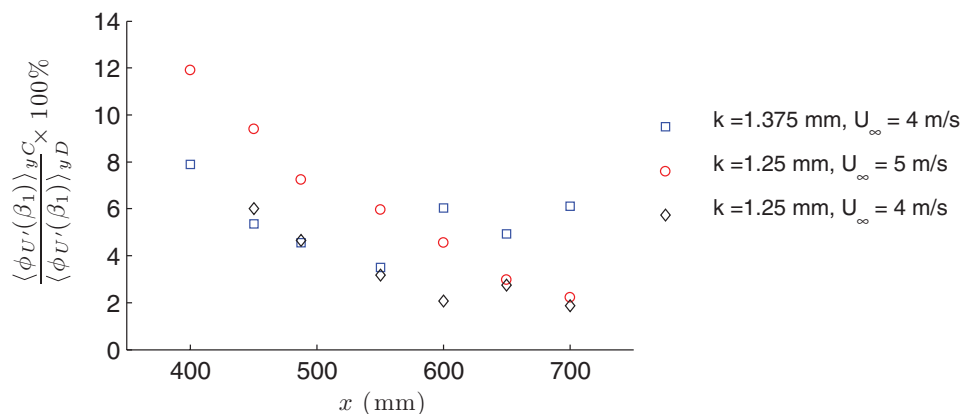


FIG. 26. The energy evolution of the β_1 mode following from Eq. (17), for the cases shown in Figure 25.

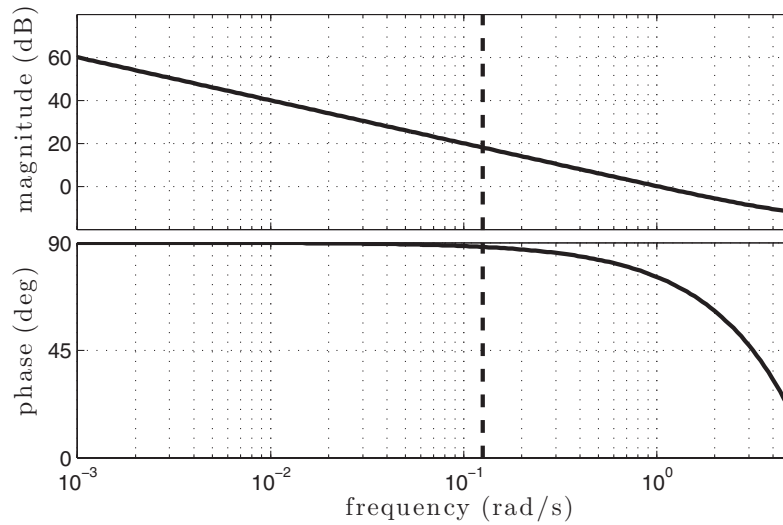


FIG. 27. Frequency response of loop gain $P'K$. The dashed vertical line marks the frequency at which the free stream velocity is varied, 0.13 rad/s.

We evaluated the controller with $K_p = K_I = 0.5 \cdot c_2 \cdot m$, which had acceptable robustness, as previously discussed in Sec. III D. The frequency response of the loop gain, $P'K$, is shown in Figure 27, and the magnitude, $|P'K|$, is large at the frequency of the velocity variation, $2\pi/T_w = 0.13$ rad/s. Therefore, since the error in rejecting disturbances is proportional to $|\frac{1}{1-P'K}|$, the disturbances were expected to be rejected effectively. For the corresponding experiment, the deviations from $\varphi_{C\tau} = 0$ are minimal with control, as shown in Figure 28 where the streamwise velocity variation is shown at the top, followed by the output of the controller, and the voltage applied to the actuator below.

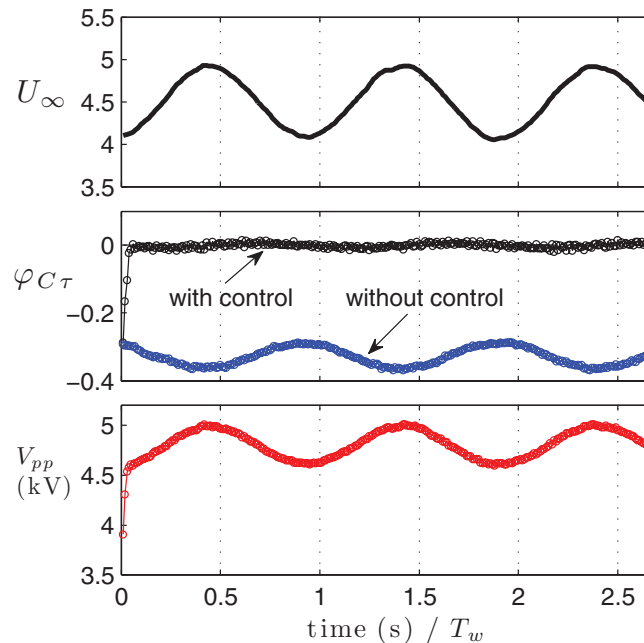


FIG. 28. Control result for a continuous velocity change with $k = 1.25$ mm and $T_w = 50$ s. The free-stream velocity is shown at the *top* with the corresponding control objective $\varphi_{C\tau}$ in the *middle*, and actuator voltage at the *bottom*.

VI. CONCLUSIONS

Control of transient growth in a Blasius boundary layer was demonstrated experimentally using a model-based feedback controller. Streamwise streaks of spanwise periodic low- and high-velocity disturbance, characteristic of bypass transition, are created with an array of cylindrical roughness elements. Farther downstream, a spanwise array of plasma actuators was arranged to generate streaks of opposite spanwise phase, to attenuate the roughness-induced disturbance and control the flow. Feedback measurements were taken with a spanwise array of wall-mounted shear-stress sensors, which were employed to sense the spanwise periodic shear-stress variations caused by roughness elements and the plasma actuators. A novel control scheme was formulated to reduce the energy in the particular spanwise wavenumber corresponding to the streaks which undergo transient growth and, if sufficiently strong, would lead to transition. Experimental data were used to find an empirical steady input-output model of the boundary layer flow, where the inputs are the disturbance caused by the roughness elements and a variable related to the driving voltage of the actuators (which results in a linearized plant model). The output was related to the measured shear stress and the targeted spanwise wavenumber (β_1). This model was used to design and analyze a proportional-integral controller prior to the implementation in the wind tunnel.

It was shown that for conditions at which the empirical model was obtained, feedback could reduce the energy associated with the targeted β_1 -mode. After control, at most 6% of residual β_1 -mode energy remained at the streamwise location where the feedback sensors were located. The cause of the remaining β_1 -mode energy could be related to the effect of aliasing on the wall-shear-stress measurements, and differences in the wall-normal distribution of the disturbance produced by the roughness versus the counter-disturbance introduced by the actuator. In contrast, the boundary-layer-averaged disturbance energy remaining over *all* wavenumbers varied between 14% and 26% for all cases considered, due to the presence of β_2 - to β_4 -modes not considered by the controller, leaving room for improvement with more intricate actuator configurations, introducing a *single* wavenumber into the flow or targeting multiple wavenumbers, and denser sensor arrays (with six to eight sensors per streak spacing) to avoid aliasing. The controller was also shown to attenuate the disturbance both upstream and downstream of the measurement plane. The effectiveness of the control strategy pursued in this study provides evidence that plasma actuators are a highly viable technology for controlling the boundary layer streaks characteristic of bypass transition.

To check the robustness of the controller, it was operated at off-design conditions by implementing the control at free-stream velocities different from that at which the input-output models were obtained. It was observed that a decrease in the free-stream velocity caused the actuator to have a stronger effect on the flow. This was attributed to the change in residence time of a fluid particle over the actuator. The controller remained highly effective at off-design conditions, even for slowly-time-varying disturbances, supporting its use in applications that have similarly slowly time-varying conditions. Any limitation of attaining the control at off-design conditions were due to shortcomings of the actuator rather than the controller. Specifically, at very low freestream velocity, the actuator had to operate at very low voltage where issues related to non-monotonic actuator characteristics were discovered.

The effectiveness of this controller demonstrates that the use of near-wall sensing, feedback, and plasma actuators are all well-suited to the control of bypass transition. Specifically, issues relating to the implementation of wall-located sensing, plasma actuators, and a suitable control objective were addressed. The next logical step is aimed at the development of low-order *dynamic* models for unsteady actuator and disturbance input. The present work addresses issues that are relevant to this next step, including the implementation of near-wall sensing and a suitable control objective. Another future direction is to combine feedforward and feedback control to increase the bandwidth of the controller. In addition, the optimal placement of actuators and sensors remains unknown, and is more effectively approached with numerical simulations.

ACKNOWLEDGMENTS

This work was supported in part by funding from the National Science and Engineering Research Council. This work was also supported in part by funding from the National Science Foundation

(Grant Nos. CMMI-0932546 and CMMI-0932928). Any opinions, findings, and conclusions or recommendations expressed are those of the authors and do not necessarily reflect the views of the National Science Foundation. R.E.H. acknowledges funding from the Queen Elizabeth II Graduate Scholarship in Science and Technology.

- ¹ W. S. Saric, H. L. Reed, and E. J. Kerschen, "Boundary-layer receptivity to freestream disturbances," *Ann. Rev. Fluid Mech.* **34**, 291–319 (2002).
- ² J. Kim and T. R. Bewley, "A linear systems approach to flow control," *Ann. Rev. Fluid Mech.* **39**, 383–417 (2007).
- ³ T. R. Bewley and S. Liu, "Optimal and robust control and estimation of linear paths to transition," *J. Fluid Mech.* **365**, 305–349 (1998).
- ⁴ M. Högberg and D. S. Henningson, "Linear optimal control applied to instabilities in spatially developing boundary layers," *J. Fluid Mech.* **470**, 151–179 (2002).
- ⁵ M. Ilak and C. W. Rowley, "Modeling of transitional channel flow using balanced proper orthogonal decomposition," *Phys. Fluids* **20**, 034103 (2008).
- ⁶ S. Bagheri and D. S. Henningson, "Transition delay using control theory," *Philos. Trans. R. Soc. A* **369**, 1365–1381 (2011).
- ⁷ M. Kerho, J. Heid, B. Kramer, and T. Ng, "Active drag reduction using selective low rate control," AIAA Paper No. 2000-4018, 2000.
- ⁸ R. Rathnasingham and K. S. Breuer, "Active control of turbulent boundary layers," *J. Fluid Mech.* **495**, 209–233 (2003).
- ⁹ S. A. Jacobson and W. C. Reynolds, "Active control of streamwise vortices and streaks in boundary layers," *J. Fluid Mech.* **360**, 179–211 (1998).
- ¹⁰ F. Lundell, "Reactive control of transition induced by free-stream turbulence: An experimental demonstration," *J. Fluid Mech.* **585**, 41–71 (2007).
- ¹¹ F. Lundell, A. Monokrousos, and L. Brandt, "Feedback control of boundary layer bypass transition: Experimental and numerical progress," AIAA Paper No. 2009-612, 2009.
- ¹² S. Grundmann and C. Tropea, "Experimental transition delay using glow-discharge plasma actuators," *Exp. Fluids* **42**, 653–657 (2007).
- ¹³ J. R. Roth, D. M. Sherman, and S. P. Wilkinson, "Electrohydrodynamic flow control with a glow-discharge surface plasma," *AIAA J.* **38**, 1166–1172 (2000).
- ¹⁴ D. M. Schatzman and F. O. Thomas, "Turbulent boundary layer separation control with plasma actuators," AIAA Paper No. 2008-4199, 2008.
- ¹⁵ A. V. Kozlov and F. O. Thomas, "Bluff-body flow control via two types of dielectric barrier discharge plasma actuation," *AIAA J.* **49**, 1919–1931 (2011).
- ¹⁶ T. Jukes and K. Choi, "Dielectric-barrier-discharge vortex generators: Characterisation and optimisation for flow separation control," *Exp. Fluids* **52**, 329–345 (2012).
- ¹⁷ K. S. Choi, T. Jukes, and R. Whalley, "Turbulent boundary-layer control with plasma actuators," *Philos. Trans. R. Soc. A* **369**, 1443–1458 (2011).
- ¹⁸ N. Bénard, J. Jolibois, E. Moreau, R. Sosa, G. Artana, and G. Touchard, "Aerodynamic plasma actuators: A directional micro-jet device," *Thin Solid Films* **516**, 6660–6667 (2008).
- ¹⁹ T. C. Corke, M. L. Post, and D. M. Orlov, "Single dielectric barrier discharge plasma enhanced aerodynamics: physics, modeling and applications," *Exp. Fluids* **46**, 1–26 (2009).
- ²⁰ E. Moreau, "Airflow control by non-thermal plasma actuators," *J. Phys. D: Appl. Phys.* **40**, 605–636 (2007).
- ²¹ R. E. Hanson, P. Lavoie, A. M. Naguib, and J. F. Morrison, "Transient growth instability cancelation by a plasma actuator array," *Exp. Fluids* **49**, 1339–1348 (2010).
- ²² R. E. Hanson, P. Lavoie, and A. M. Naguib, "Effect of plasma actuator excitation for controlling bypass transition in boundary layers," AIAA Paper No. 2010-1091, 2010.
- ²³ L. P. Osmokrovic, R. E. Hanson, and P. Lavoie, "Effect of DBD plasma actuator geometry and excitation for producing transient growth modes in a laminar boundary layer," AIAA Paper No. 2012-2944, 2012.
- ²⁴ E. B. White, "Transient growth of stationary disturbances in a flat plate boundary layer," *Phys. Fluids* **14**, 4429–4439 (2002).
- ²⁵ J. H. M. Fransson and L. Brandt, "Experimental and theoretical investigation of the nonmodal growth of steady streaks in a flat plate boundary layer," *Phys. Fluids* **16**, 3627–3638 (2004).
- ²⁶ E. B. White, J. M. Rice, and F. Gökhan Ergin, "Receptivity of stationary transient disturbances to surface roughness," *Phys. Fluids* **17**, 064109 (2005).
- ²⁷ P. Lavoie, A. Naguib, and J. Morrison, "Transient growth induced by surface roughness in a blasius boundary layer," in *Mechanics Down Under—Proceedings of the 22nd International Congress of Theoretical and Applied Mechanics* (Springer, Adelaide, Australia, 2008), p. 12158.
- ²⁸ M. Gaster, "Active control of laminar boundary layer disturbances," in *IUTAM Symposium on Flow Control and MEMS*, edited by J. F. Morrison, D. M. Birch, and P. Lavoie, IUTAM Symposium London, England (Springer, 2006).
- ²⁹ J. Kim and J. Lim, "A linear process in wall-bounded turbulent shear flows," *Phys. Fluids* **12**, 1885–1888 (2000).
- ³⁰ W. S. Saric, "Boundary-layer stability and transition," in *Springer Handbook of Experimental Fluid Mechanics*, edited by C. Tropea, A. Yarin, and J. Foss (Springer, Berlin-Heidelberg, 2007), Chap. 12.3, pp. 886–896.
- ³¹ R. E. Hanson, H. P. Buckley, and P. Lavoie, "Aerodynamic optimization of the flat-plate leading edge for experimental studies of laminar and transitional boundary layers," *Exp. Fluids* **53**, 863–871 (2012).
- ³² A. Abdel-Rahman, C. Tropea, P. Slawson, and A. Strong, "On temperature compensation in hot-wire anemometry," *J. Phys. E: Sci. Instrum.* **20**, 315–319 (1987).
- ³³ R. J. Moffat, "Describing the uncertainties in experimental results," *Exp. Thermal Fluid Sci.* **1**, 3–17 (1988).
- ³⁴ J. R. Taylor, *Introduction to Error Analysis*, 2nd ed. (University Science Books, 1997).

- ³⁵ N. M. Houser, L. Gimeno, R. E. Hanson, T. Goldhawk, T. Simpson, and P. Lavoie, "Microfabrication of dielectric barrier discharge plasma actuators for flow control," *Sens. Actuators A: Phys.* **201**, 101–104 (2013).
- ³⁶ A. M. Naguib, J. F. Morrison, and T. A. Zaki, "On the relationship between the wall-shear-stress and transient-growth disturbances in a laminar boundary layer," *Phys. Fluids* **22**, 054103 (2010).
- ³⁷ G. Comte-Bellot, "Hot-wire anemometry," *Ann. Rev. Fluid Mech.* **8**, 209–231 (1976).
- ³⁸ H. H. Fernholz, G. Janke, M. Schober, P. M. Wagner, and D. Warnack, "New developments and applications of skin-friction measuring techniques," *Meas. Sci. Technol.* **7**, 1396–1409 (1996).
- ³⁹ R. E. Hanson, P. Lavoie, K. M. Bade, and A. M. Naguib, "Steady-state closed-loop control of bypass boundary steady-state closed-loop control of bypass boundary layer transition using plasma actuators," AIAA Paper No. 2012-1140, 2012.
- ⁴⁰ K. J. Åström and R. M. Murray, *Feedback Systems: An Introduction for Scientists and Engineers* (Princeton University Press, 2008).
- ⁴¹ S. Skogestad and I. Postlethwaite, *Multivariable Feedback Control, Analysis and Design*, 2nd ed. (John Wiley & Sons Ltd., 2005).